AIAA JOURNAL
Vol. 45, No. 7, July 2007

Zonal-Detached-Eddy Simulation of Projectiles in the Subsonic and Transonic Regimes

Franck Simon,* Sébastien Deck,† and Philippe Guillen†
ONERA, 92322 Châtillon Cedex, France
Roxan Cayzac‡
Nexter Munitions, 18023 Bourges Cedex, France
and
Alain Merlen§
Université des Sciences et Technologies de Lille, 59655 Villeneuve d'Asq Cedex, France

DOI: 10.2514/1.26827

This paper presents nonspinning-projectile computations with advanced turbulence modeling to demonstrate the relevance of using a hybrid method in projectile simulations. A zonal-detached-eddy simulation methodology is used to improve the base-flow prediction without deteriorating the incoming attached flow upstream of the base in the subsonic and transonic regimes. The numerical results are found to compare fairly well with the available experimental wall-pressure data. Both time-averaged and unsteady features are then discussed. Particular attention was paid to the near-wake flowfield and its dependency upon the freestream Mach number. In these calculations, some classical features of massively separated flows, such as the pressure evolution along the base or the wake centerline characteristics, are poorly predicted with the Spalart–Allmaras model. The use of a hybrid method leads to promising results and allows for a physical analysis of the separated flowfield. The flow appears to exhibit self-similar properties, even in the recirculation area, independently of the Mach number value in the range of freestream conditions investigated. Moreover, the instability process leading to the shear-layer growth is found to be similar in the range of parameters investigated and is in accordance with previous results concerning the compressibility effects in free shear flows. Finally, base-pressure spectra are reported and compared with axisymmetric base-flow data.

Introduction

THE understanding of spinning-projectile aeroballistics is a challenging task due to the diversity of their flight conditions and to very specific issues such as the influence of the body rotation, imposed by stability criteria. In the past, many studies have been devoted to projectile computations to validate turbulence models and to get further insight into the physics of such flows. A wide range of freestream conditions was investigated, from the subsonic [1–4] to the supersonic regime [2,5–7]. Despite the improvement of the one-equation Spalart–Allmaras [8,9] results compared with those obtained with the algebraic Baldwin–Lomax model [10], shortcomings of statistical turbulence models were evidenced under special flight conditions [11,12], requiring a more advanced modeling approach. In particular, the body rotation of spin-stabilized projectiles combined with nonzero angle of attack in the transonic regime has proven to be a difficult exercise for Reynolds-averaged Navier–Stokes (RANS) models [11].

In addition, the active flow control field has recently encountered great advances [13], mainly in the knowledge of device fabrication with the use of the microelectromechanical systems (MEMS) technology. Until very recently, base flow control studies were focused on reducing base drag. For example, fluidic control known as base bleed [14–19] and a modification of the base geometry with the addition of a cavity [20,21] have demonstrated their capacity to achieve some control. However, new concepts under studies dealing with improved maneuverability involve very low-scale actuators. Such an example can be found in the numerical work of Sahu [22–25] in which a synthetic jet is used to generate aerodynamic forces during flight by locally reattaching the separated flow over a Coanda surface located at the base. The feasibility of such control was also demonstrated with the experiments of Rinehart et al. [26] and McMichael et al. [27]; however, it involves the capability of accurately predicting the unsteady flow around the control device while computing the whole projectile configuration at high Reynolds number.

Most of the modeling difficulties are thus concentrated in the near-wake area due to the existence of large-scale unsteadiness (see, for example, Motallebi and Norbury [28]) responsible for the failure of several statistical turbulence models to reproduce the flow physics. To assess this critical issue, efforts have to be made to resolve the dynamics of the coherent vortices in the recirculating region through the use of an advanced turbulence modeling strategy such as large-eddy simulation (LES).

This constitutes the purpose of the present study, for which the objectives are twofold: first, to demonstrate the relevance of hybrid RANS/LES methods to perform simulations of projectile base flows; second, to get a better insight into the turbulent flow structure in the subsonic and transonic regimes. Thus, a zonal-detached-eddy simulation (ZDES) methodology was used to perform simulations around a secant-ogive-cylinder boat-tail projectile (SOCBT) for several freestream Mach numbers ranging from 0.50 to 1.05. The numerical procedure and the simulations performed are first described. A validation of the attached flow along the projectile is then presented from wall-pressure comparisons with available experimental data. The time-averaged flowfields on the projectile and in the near wake are then investigated. Instantaneous

Received 27 July 2006; revision received 9 January 2007; accepted for publication 5 February 2007.

*Ph.D. Student, Applied Aerodynamics Department, B.P. 72, 29 Avenue de la Division Leclerc; franck.simon@onera.fr.
†Research Engineer, Applied Aerodynamics Department, B.P. 72, 29 Avenue de la Division Leclerc.
‡Research Engineer, Département Balistique et Contrôle du Vol, 7 Route de Guerry.
§Professor, Laboratoire de Mécanique, Bât M3, Cité Scientifique.

visualizations are also used to describe the unsteady features of such flows. Finally, a spectral analysis of the base-pressure fluctuations is achieved.

Numerical Procedure

Code

The multiblock Navier–Stokes solver used in the present study is the FLU3M code developed by ONERA. The equations are discretized using a second-order-accurate, upwind, finite volume scheme and a cell-centered discretization. The Euler fluxes are discretized by a classical Roe scheme. The solution is advanced in time using a second-order-accurate implicit scheme with Newton-type inner iterations. Further details concerning the numerical procedure and the turbulence modeling may be found in Péchier et al. [6] and Deck et al. [29]. The FLU3M code was already used on a wide range of configurations similar to those used in the present study. For example, subsonic base-flow [30] and projectile configurations in the subsonic regime [11] and in the supersonic regime [6,7] were already successfully investigated.

Turbulence Modeling

The direct-eddy-simulation (DES) approach [31] is originally based on the RANS one-equation turbulence model of Spalart–Allmaras [8,9]. The main idea is to perform RANS calculation in attached boundary layers in which RANS models are known to behave quite well and to switch to an LES accuracy in the separated regions. The passage from one mode to another is piloted by a length parameter governed by $\min(d, C_{\mathrm{DES}}\Delta)$, where d is the distance to the wall, Δ is a characteristic length of the computational cell, and C_{DES} is a constant, equal to 0.65 [32]. Close to the wall, $d < C_{\mathrm{DES}}\Delta$ and the model behaves as the classical RANS Spalart–Allmaras model. Far away from the wall, $d > C_{\mathrm{DES}}\Delta$ and the model behaves in LES mode with an equivalent subgrid-scale model. A derived method, called zonal-detached-eddy simulation , appears to be well adapted for flows with separation fixed by the geometry, by allowing the user to combine RANS and DES methods. Indeed, ZDES differs from standard DES in spirit by the fact that the user selects individual RANS and LES domains. One of the interests of the ZDES approach is that the user can focus grid refinement on regions of interest (e.g., base region) without corrupting upstream boundary layers by grid-induced separation (GIS) [36] when structure grids are used. This is actually the case for projectiles at low angle of attack for which separation appears only at the base. This justifies the use of the ZDES approach in the present study, in which an unsteady RANS (URANS) method is employed upstream of the base, whereas a DES methodology is used downstream. Nevertheless, other approaches, such as the recently proposed delayed-detached-eddy simulation (DDES) [37], are also an alternate to avoid GIS. For a deeper discussion on hybrid RANS/LES methods, see the review by Sagaut et al. [38].

Simulation Overview

The geometry used in the present study is the classical SOCBT configuration, which consists of a 6-caliber projectile length with a 3-caliber ogive, a 1-caliber boat-tail, and secant junctions with the cylinder. This particular configuration was chosen from the published experimental data available. Thus, measurements of wall pressure on the body and global coefficients were achieved , allowing for a validation of the projectile flow on a wide range of freestream conditions in the transonic regime.

The mesh used in the present study was generated with MESH3D software [40] and is fully three-dimensional. The boundaries of the computational domain are, respectively, set to $20D$ upstream of the projectile and $30D$ downstream. The radial extend is equal to $30D$. The same mesh was used in RANS and ZDES simulations to allow for direct comparisons. The total number of cells is approximately equal to 7.6 million. Figure 1a depicts a view of the mesh around the projectile in the x–y plane. The developing turbulent boundary layer

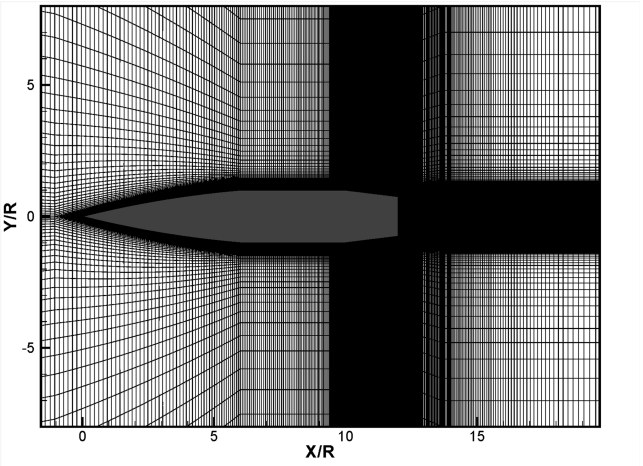

a) Mesh around projectile

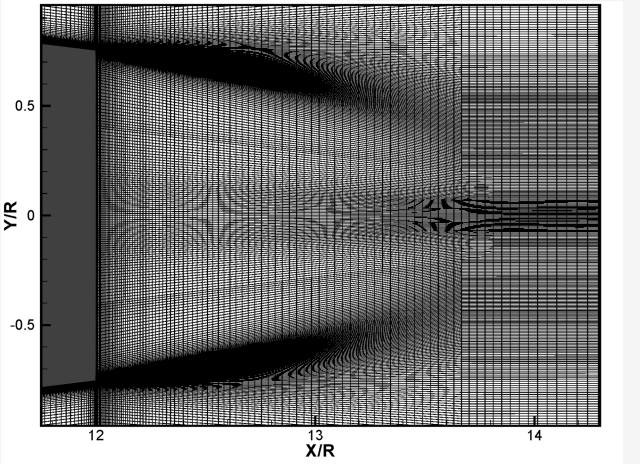

b) Basic grid area in the x–y plane

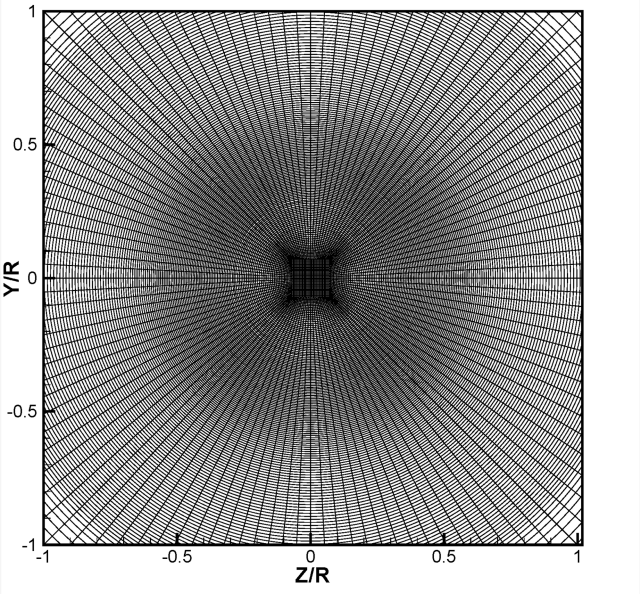

c) Detailed view of the mesh in the rear stagnation area in the y–z plane

Fig. 1 Computational mesh.

is discretized by approximately 40 cells in the radial direction on the cylinder, which leads to a height nearly equal to $\delta/R \sim 7\%$. On the boat tail, the boundary layer thickens and reaches a value of $\delta/R \sim 17\%$ for the $M_\infty = 0.7$ case at the separation point. It can be noted that the longitudinal discretization is well beyond that required by the RANS approach, because 255 cells are used to capture the

Table 1 Simulations overview

Method	M_∞	α
RANS	0.5	0
RANS	0.7	0
RANS	0.91	2
RANS	0.91	10
RANS	0.96	0
RANS	0.96	4
RANS	1.05	0
RANS	1.20	6
ZDES	0.5	0
ZDES	0.7	0
ZDES	0.91	0
ZDES	1.05	0

streamwise evolution of the boundary layer. Moreover, to properly capture the instability process of the separated shear layer behind the base, an azimuthal resolution of 3 deg by plane was adopted, leading to a number of 120 cells. In fact, as previously mentioned, the present study is a first attempt in the use of ZDES for projectile computations. Further work will follow concerning the combination of body rotation and angle of attack, and the same mesh will be used. Moreover, active control studies currently under investigation will also require adapted density grids.

The use of a ZDES methodology can be justified by two observations made in previous studies. First, RANS calculations are sufficient to properly simulate the flow on the projectile if the turbulent boundary layer remains attached. Second, most turbulence models fail to predict the massively separated flowfield behind the base [7,35,41]. This comes mainly from the fact that dominant eddies in massively separated flows are highly geometric dependent and have not much in common with the eddies in thin shear flows that classical RANS models are designed to mimic (see the discussion by Sagaut et al. [38]). However, advanced unsteady methods such as DES have demonstrated their superiority in predicting afterbody flows [41,42]. The ZDES approach, in such cases, combines the superiority of both RANS and DES methods in their respective fields, because any modeled stress depletion (see Spalart et al. [37]) issue is avoided. Because of the use of a ZDES approach, the incoming flow is treated at a reasonable cost in URANS mode upstream of the base without loss of prediction accuracy. For downstream separation, the recirculating area exhibits large-scale unsteadiness, thus needing to be treated in DES (LES mode). In the near wake, small isotropic cells (as far as possible) are required, as in classical LES simulations. This justifies the particular attention paid to the meshing strategy in this area. Figure 1b displays a close view of the refining strategy in the high-gradient region occurring behind the base. An O–H topology was used (cf. Fig. 1c) to avoid convergence difficulties of the inner-iterations algorithm on the axis.

The RANS simulations were performed on a variety of Mach numbers and angles of attack to compare to the available experiments. After this validation exercise, ZDES calculations are used to investigate the dependency of the flow on the freestream Mach number. All of the simulations, which are shown in Table 1, were performed with $P_i = 100$ kPa and $T_i = 320$ K, leading to a Reynolds number Re_L based on the freestream velocity U_∞ and the projectile length L ranging from 3.3×10^6 to 4.4×10^6, depending on the M_∞ value.

All simulations were achieved with the spatial Roe scheme with a Harten coefficient Ψ, respectively, equal to 0.1 in the RANS cases (with a Minmod limiter) and to 0.01 in the ZDES cases (third-order, upwind-biased). This change in the numerical parameters allows for reducing the numerical dissipation in the separated region when the hybrid methodology is used. For the unsteady simulations, the time integration was performed with the gear scheme and a time step equal to 8×10^{-7} s, coupled with four Newton subiterations.

The drag coefficient C_D evolution was monitored during the simulations. Once C_D has achieved a quasi-steady state (in a statistical sense), the transient phase was considered to be over and the time-averaged statistics were gathered. Based on the existence of a vortex-shedding phenomena at reduced frequency $St_D = 0.2$, statistics were collected during 45 to 75 periods, depending on the freestream Mach number.

Results and Discussion

Validation

The simulations are first compared with the available pressure measurements [1,39]. As previously mentioned, the use of a zonal method allows for using the RANS mode on the whole projectile body. Thus, because no separation occurs in the range of parameters used in the present study, the attached boundary layer is treated in RANS mode, which was proved to be sufficient for such flows. Comparisons with experiments were performed for all simulations matching the experimental conditions. Four examples, among all of the RANS results, are depicted in Fig. 2 for different Mach numbers and angles.

Numerical results are in quantitative agreement with the experimental data, because the high-pressure-gradient regions are well captured by the computations, meaning that shocks and expansion fans are properly resolved. Although not shown here, the other simulations performed at different Mach numbers and angles of attack display similar accuracy levels. This validation reinforces the justification of using a RANS approach on the projectile body (excluding the base).

Mach Number Dependency

Because computations are thought to properly match the experimental data (see the previous section), the physics involved in the subsonic and transonic regimes are investigated from both the time-averaged and instantaneous points of view.

Mean Flow Around the Projectile

The time-averaged flowfield on the body is first investigated to evidence the physics changes that depend upon the Mach number.

Figures 3 and 4 present, respectively, the isocontours of pressure and the streamwise evolution of the pressure coefficient along the projectile body for the four ZDES simulations. The $M_\infty = 0.50$ and $M_\infty = 0.70$ cases exhibit the same behavior. The incoming flow decelerates due to the upstream influence of the projectile nose. The flow then accelerates along the ogive, involving a decrease in the pressure coefficient. The secant junctions, first between the ogive and the cylinder and then between the cylinder and the boat tail, are responsible for a rapid change in the pressure level. However, the subsonic nature of the flow allows for a quick recovery of the pressure downstream of both geometrical junctions (see Fig. 4). Despite the stronger pressure gradient in the $M_\infty = 0.70$ case, the streamwise evolution of the nondimensionalized pressure coefficient is similar for the two cases. The $M_\infty = 0.91$ case is quite different due to the transonic freestream conditions. Despite a similar evolution on the ogive, the flow exhibits a stronger acceleration on the body, leading to the appearance of two shocks on the cylinder and on the boat-tail sections. These transonic features are responsible for a slower pressure recovery at both geometrical junctions. The fourth case departs from the subsonic and transonic cases, due to the supersonic freestream Mach number. A conical oblique shock appears at the nose, due to the lack of upstream disturbances from the supersonic flow. The C_p level on the ogive increases compared with the previous simulations. The supersonic incoming flow leads to the formation of expansion fans at both geometrical junctions. Past the expansions, the pressure recovery is very slow compared with that encountered in the subsonic regime, and the whole cylinder length is required to reach a pressure coefficient nearly equal to that observed just upstream of the expansion. The wall-pressure increases linearly on the boat tail, contrary to the pressure evolution encountered in the subsonic and the transonic regimes.

The streamwise evolution of the total drag coefficient was calculated and is plotted in Fig. 5. As previously observed for the isopressure contours, both subsonic cases display the same drag

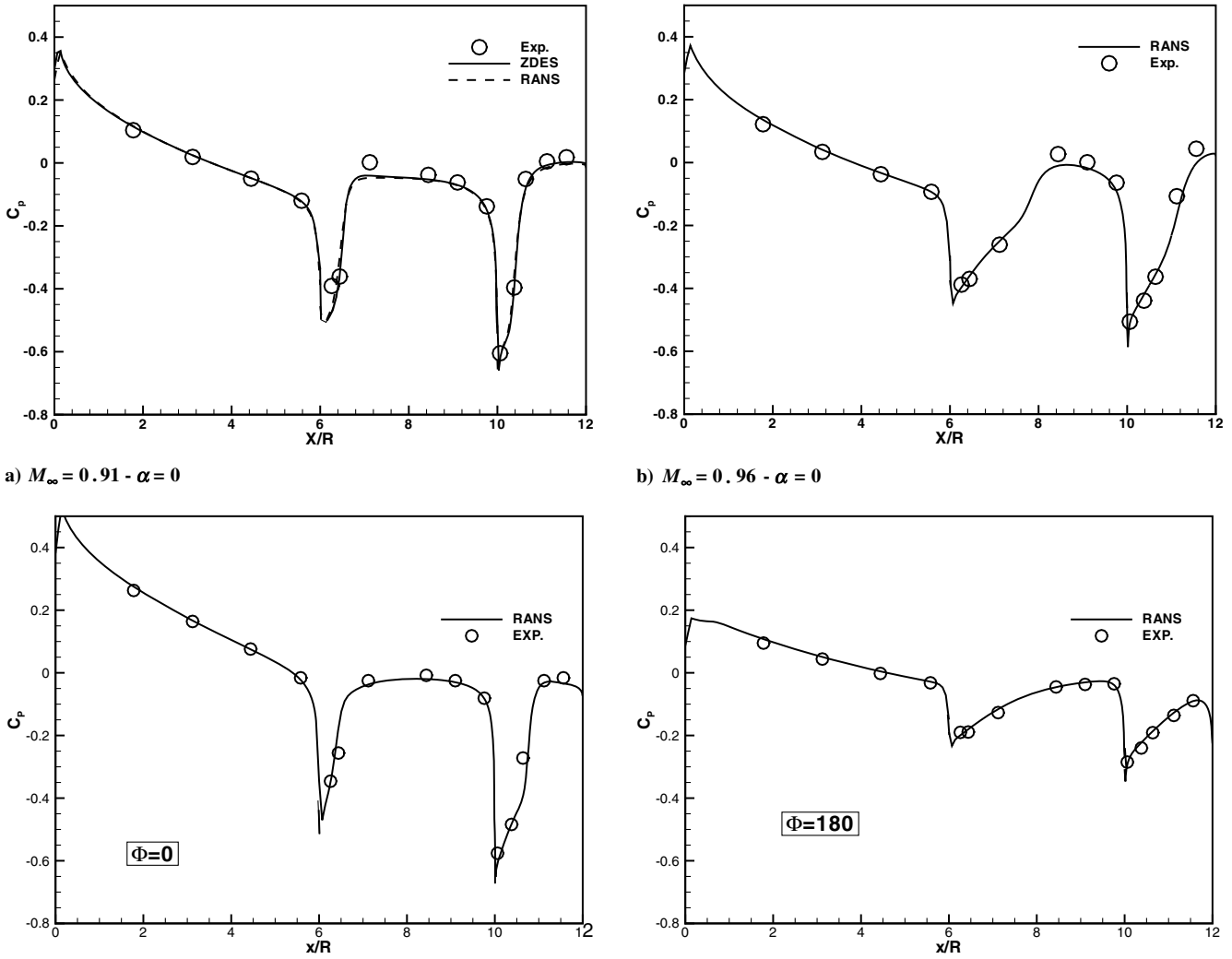

a) $M_\infty = 0.91$ - $\alpha = 0$

b) $M_\infty = 0.96$ - $\alpha = 0$

c) $M_\infty = 0.91$ - $\alpha = 10$ - $\Phi = 0$ (wind side)

d) $M_\infty = 1.20$ - $\alpha = 6$ - $\Phi = 180$ (lee side)

Fig. 2 Longitudinal evolution of the wall pressure along the projectile, compared with experiments [39].

coefficient as quite identical pressure evolution occurs. Thus, for subsonic cases without shock waves on the body, the total drag level and evolution are similar. When M_∞ raises to transonic values, the shock waves appearing on the body lead to drastically higher drag values on the boat tail. When M_∞ is supersonic, the conical shock at the projectile nose deeply modifies the evolution of the axial force coefficient. Thus, at the ogive-cylinder junction, the drag is approximately four times higher than in the subsonic cases at the same location and is even higher than the drag coefficient on the whole subsonic projectile. On the cylinder part, notice that the drag evolution is identical in the four cases. As for the $M_\infty = 0.91$ case, the $M_\infty = 1.05$ case leads to a very high drag level on the boat tail, because the total drag is twice higher than in the transonic case.

Further investigation was achieved in Fig. 6 by distinguishing the pressure and viscous drag components of the total drag. It can be observed that the discrepancies highlighted between the four cases in the total drag are mainly due to different pressure-drag evolution. Because the angle of attack is equal to zero, the pressure drag remains constant on the whole cylinder length. Thus, the pressure evolution along the ogive and the boat tail is responsible for the higher pressure drag. The appearance of shocks in the transonic regime involves a rapid increase of the pressure drag along the boat tail, compared with the subsonic cases. In the supersonic regime, the attached conical shock at the nose leads to a quite different pressure-drag evolution along the ogive. Moreover, the supersonic freestream conditions are responsible for an important raise of the drag pressure coefficient along the boat tail. Thus, in the transonic case, the discrepancies with the subsonic regime appear on the boat tail, whereas in the supersonic regime, both the ogive and the boat tail are responsible for the increase of the pressure drag. Concerning the viscous component, the drag evolution along the body is quite similar for the different freestream conditions. However, the viscous drag slightly increases in the transonic and the supersonic cases, due to the thickening of the boundary layer on both the cylinder and the boat tail.

Near-Wake Behavior

Available experimental data concerning axisymmetric base flows are quite sparse due to the difficulties of making reliable measurements in the separated flow behind the base without introducing any perturbations. Thus, particular attention was paid to numerically investigating the near-wake behavior.

Figure 7 presents the iso-Mach number contours and the isopressure lines. Computed streamlines were added to evidence the location of the rear stagnation point and some flow properties of interest are gathered in Table 2, including the recirculation length L_R, the maximum backflow velocity U_{axis}/U_∞, the convective Mach number M_c, and the estimated isentropic convective velocity U_c/U_∞. The flow topology appears to be quite similar for the three lower M_∞ cases in which no shock occurs in the base region. It can be noted that the recirculation area extent L_R increases with M_∞, as in the blunt-base-flow [43,44] studies. The maximum backflow velocity corroborates with earlier findings in massively separated flows [43,44]. The convective Mach number [45,46] M_c stays below 0.6, indicating that the mixing layer originating from the base is not subject to strong compressibility effects. The maximum level of streamwise and radial velocity fluctuations were also added.

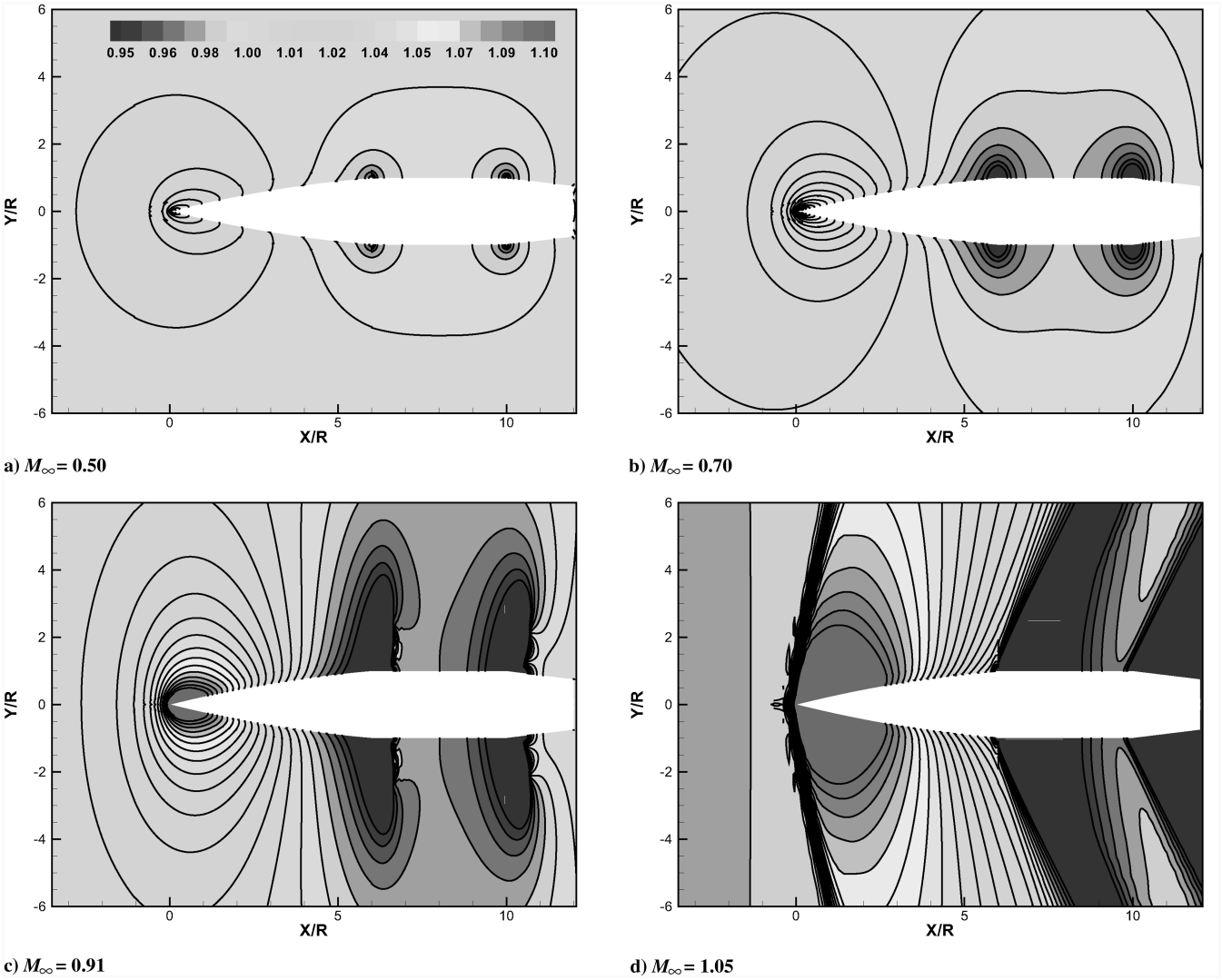

Fig. 3 Time-averaged flow behavior; isocontours of P/P_∞ ratio.

The centerline velocity in the wake is displayed in Fig. 8. Some ZDES results from Deck [41] and Simon [47] concerning axisymmetric blunt-base configurations in the subsonic regime were also used to provide a point of comparison ($M_\infty = 0.70$). The empirical law of Merz [43], based on experimental data at several subsonic Mach numbers (from 0.2 to 0.85), was added to the present results and reads as follows:

$$u/U_{c_{\max}} = \sin^m[\pi(x/L_R)^n] \tag{1}$$

with $m = 0.612949$ and $n = 1.356915$. It is observed that the maximum backflow velocity $U_{c_{\max}}$ occurs at the same location for all

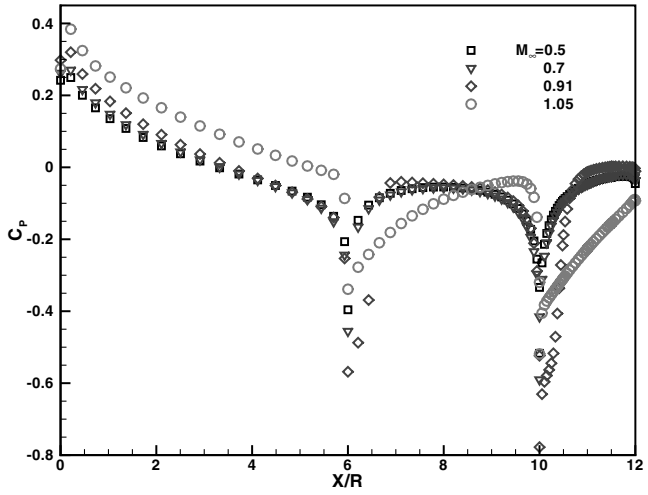

Fig. 4 Longitudinal evolution of the pressure coefficient K_p along the projectile.

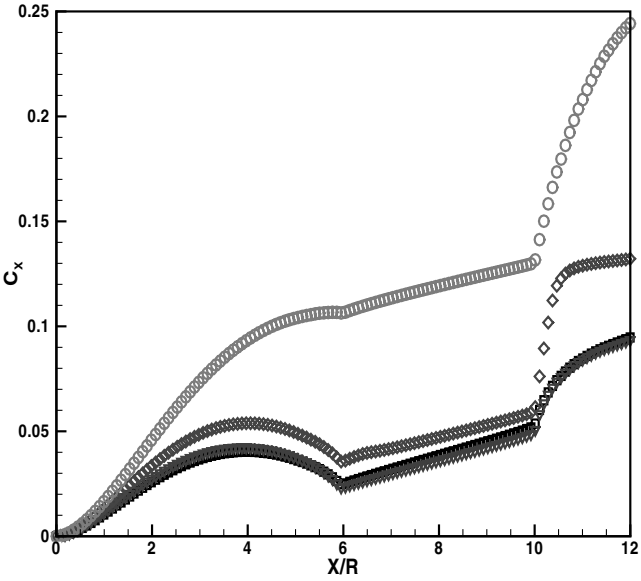

Fig. 5 Streamwise integration of the total drag coefficient (see Fig. 4 for the legends).

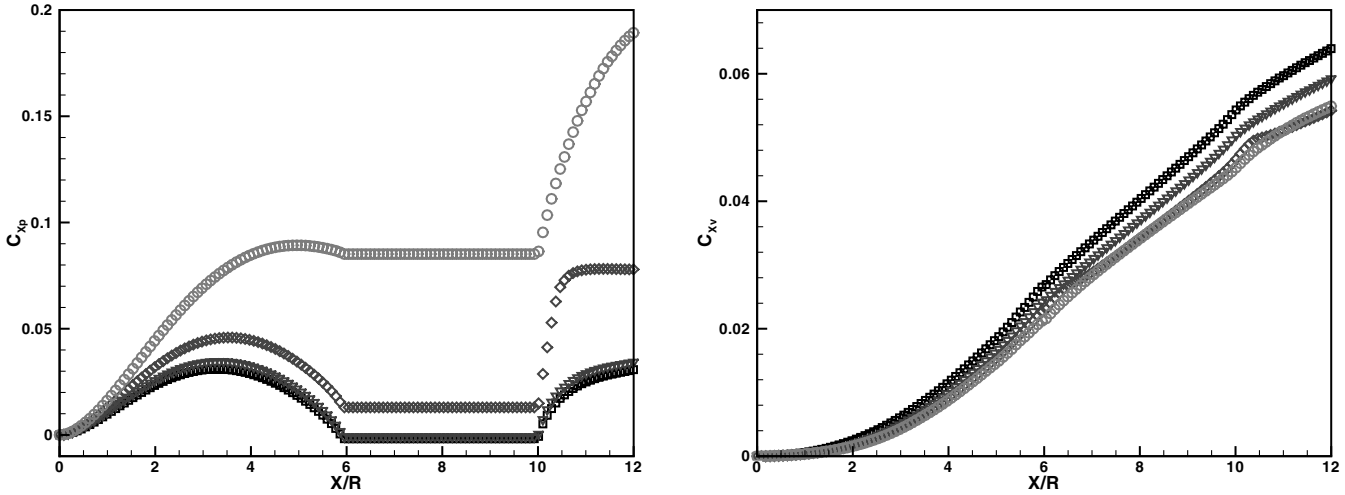

a) Pressure component **b) Viscous component**

Fig. 6 Streamwise integration of the drag components (see Fig. 4 for the legends).

of the ZDES cases, which is approximately equal to 60% of the recirculation extent. Moreover, the maximum reverse flow is nearly equal to 30% of U_∞ for all cases (see Table 1). Note that all of the present RANS simulations failed to reproduce the wake-velocity evolution.

Another relevant parameter for investigating base flows is the centerline pressure coefficient, which was plotted in Fig. 9 for the four cases. Both RANS and ZDES results are shown to compare the predicted flow topologies. Because of the lack of experimental data, some additional results were added. The wind-tunnel data of Merz

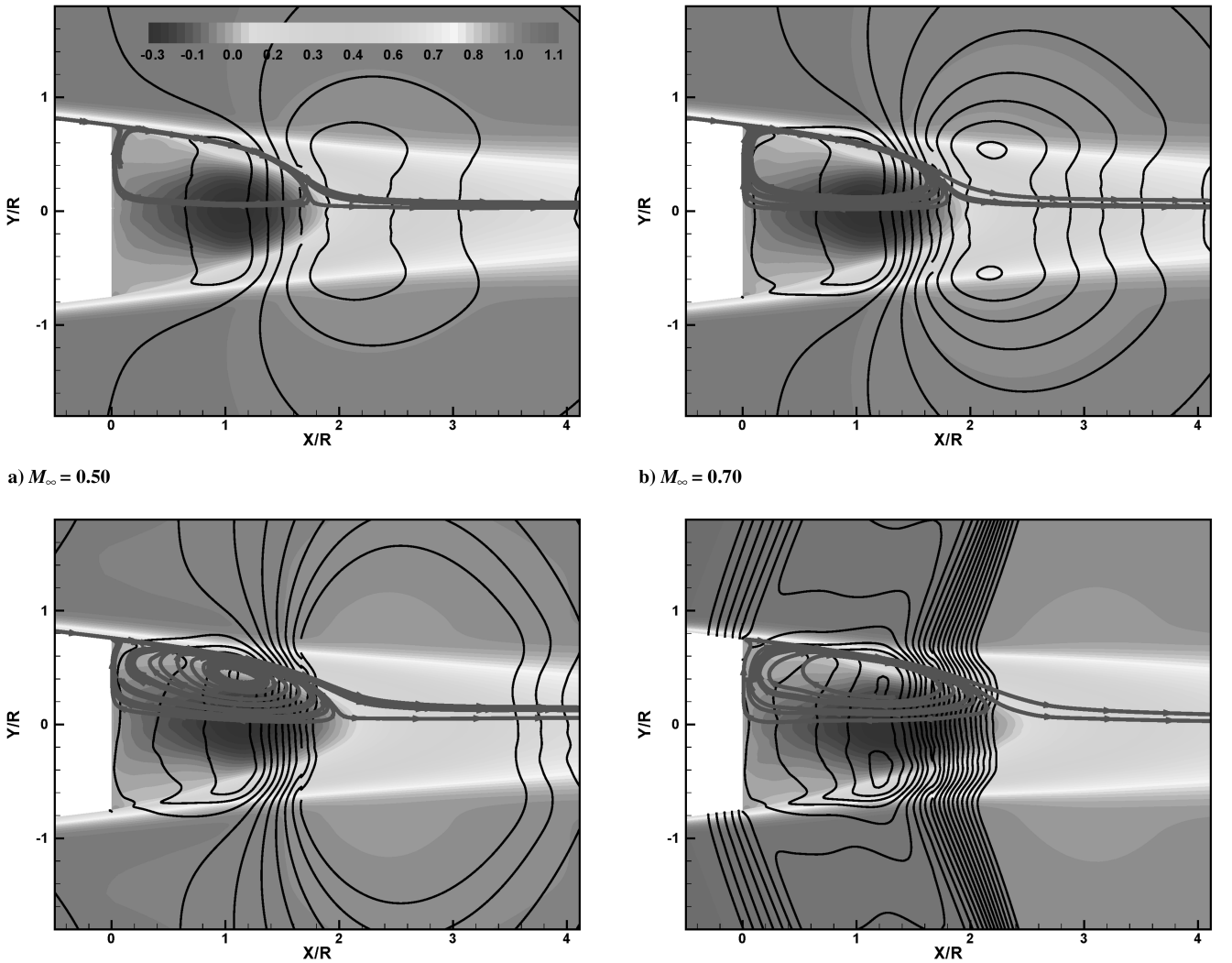

a) $M_\infty = 0.50$ **b)** $M_\infty = 0.70$

c) $M_\infty = 0.91$ **d)** $M_\infty = 1.05$

Fig. 7 Time-averaged base-flow behavior; iso-Mach number contours, isopressure lines and computed streamlines.

Table 2 Summary of base-flow properties in ZDES simulations

M_∞	$\langle C_p \rangle$	L_R/R	$U_{\text{axis}_{\max}}/U_\infty$	M_c	U_c/U_∞	$u^2_{\text{rms}}/\Delta U^2$	$v^2_{\text{rms}}/\Delta U^2$
0.50	−0.027	1.77	27%	0.25	51%	0.027	0.032
0.70	−0.021	1.84	28%	0.35	51%	0.027	0.029
0.91	0.0005	1.99	27%	0.43	51%	0.027	0.026
1.05	−0.079	2.27	29%	0.53	52%	0.034	0.026

[43] and ZDES results from Deck [41] and Simon [47] concerning axisymmetric blunt-base configurations in the subsonic regime were used.

It is obvious that the pressure evolution in the recirculating area differs from that encountered in the axisymmetric case of Merz , even if the data collapse in the turbulent developing wake. The discrepancies occur before the rear stagnation point. They may be due to the addition of a boat tail in the present case, leading to an alteration of the flowfield. In the present cases, the streamlines curvature is only slightly affected by the separation process at the base, compared with the blunt-base case. Thus, the equilibrium between the freestream and the recirculating flow is modified, responsible for the differences observed in Fig. 9 between the present simulations and the experimental data. The numerical results display similar trends, despite different base-pressure levels.

From an industrial point of view, the base-pressure predictions are of practical importance, because base drag can be a major contribution to the total drag of the projectile. The base-pressure coefficient is depicted in Fig. 10 for all Mach numbers. The four cases exhibit a flat pressure profile, which is a common feature of base flows in the subsonic regime [48] and in the supersonic regime [49]. However, this important property is not properly reproduced by RANS calculations, which leads to strong radial variation of the base pressure. For the sake of clarity, only one RANS result was plotted in Fig. 10. It is obvious that the SA model fails to predict the flat profile, as previously observed in both the supersonic [35,50] and the subsonic regime [41]. This result highlights the relevance of using a hybrid method. For both subsonic ZDES cases, the base-pressure coefficients are quite similar. For the $M_\infty = 1.05$ case, the C_p value drops, due to the supersonic freestream conditions leading to the appearance of expansion fans on the body (see Fig. 3). The transonic result ($M_\infty = 0.91$ case) is quite astonishing,because it leads to a nearly zero base drag. This result agrees well with the experimental measurement of Kayser [51], who observes a C_p value of nearly 0.01. This particular behavior is due to the pressure history on the projectile body, as previously described. Indeed, the appearance of shock waves on the body allows for a recovery of the freestream pressure at the base. Kayser reported a positive base-drag coefficient for freestream Mach number ranging from 0.91 to 0.98, which highlights the particularity of the transonic regime concerning the base pressure. However, the total drag increases drastically in the transonic regime, due to the compression occurring on the body. Finally, it can be noted that such results can hardly be compared with classical base-flow results, because the base-pressure coefficient is highly dependent on the pressure history on the body before separation.

The radial evolution of the pressure fluctuations was also investigated (Fig. 11). It can be observed that the level of fluctuations increases with M_∞. For the lower subsonic case, the fluctuations are nearly constant on a radius, contrary to the higher M_∞ cases in which maximum of pressure fluctuations is reached at the center. This is in accordance with previous observations dealing with subsonic base-pressure studies [48,52]. It can, however, be noted that it differs from the supersonic case in which fluctuations are found to increase from the base center to the outer part and reach their maximum at approximately $r/R \sim 0.7$ [49]. The level of maximum base-pressure fluctuations is found to quickly increase in the transonic regime, in accordance with the numerical prediction of Kawai [53] concerning a blunt-base axisymmetric flow. It can be noted that Kawai performed

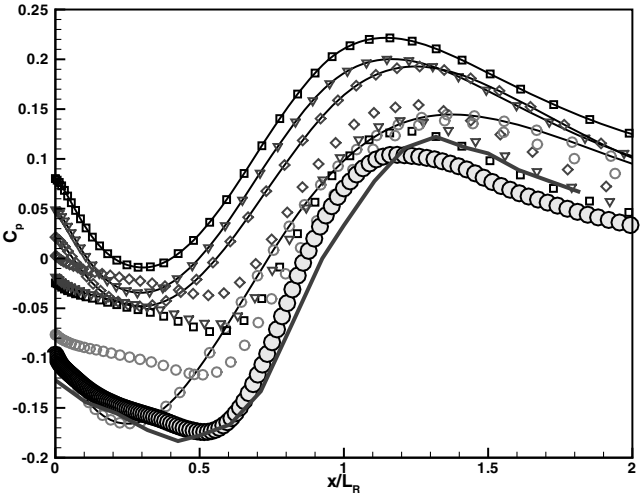

Fig. 9 Longitudinal evolution of the pressure coefficient along the centerline (see Fig. 8 for the legends).

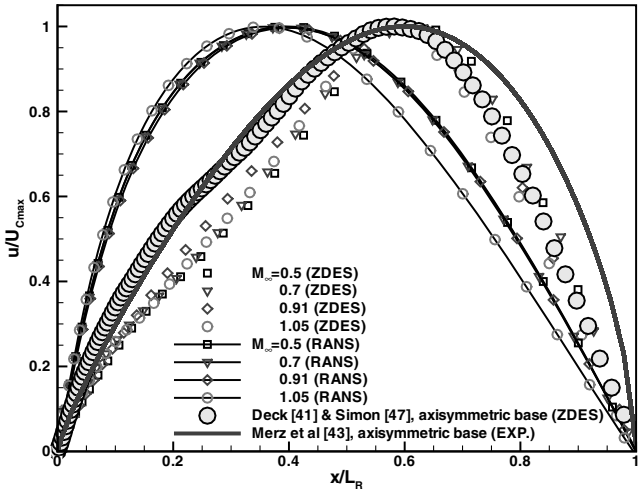

Fig. 8 Longitudinal evolution of the centerline velocity in the separated flow behind the base.

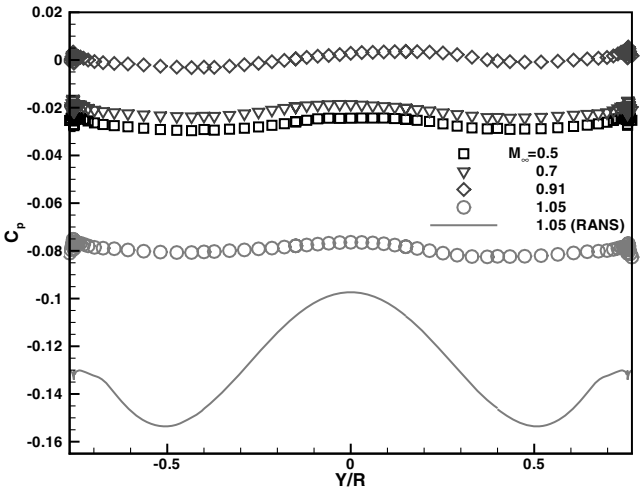

Fig. 10 Radial evolution of the base-pressure coefficient.

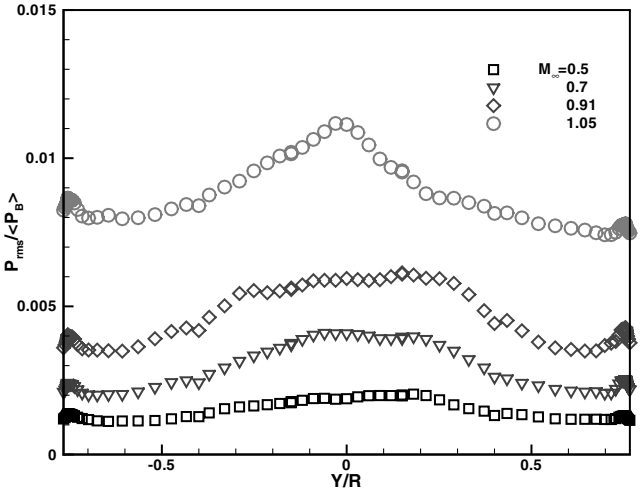

Fig. 11 Radial evolution of the base-pressure fluctuations.

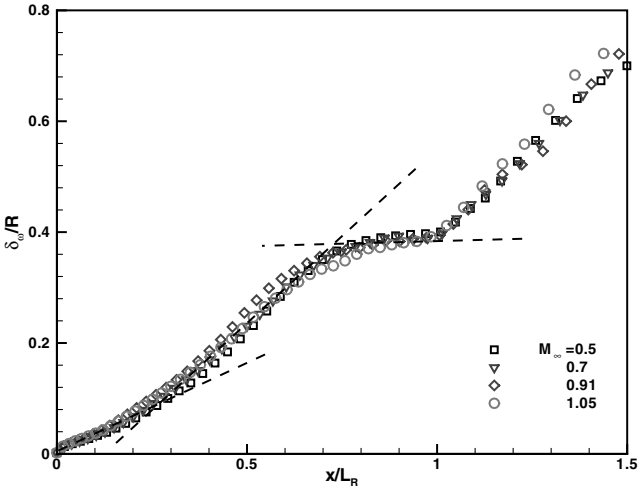

Fig. 12 Evolution of the vorticity thickness δ_w.

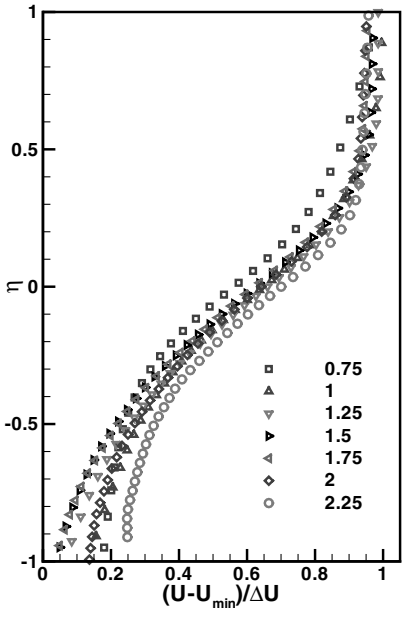

a) $M_\infty = 0.50$

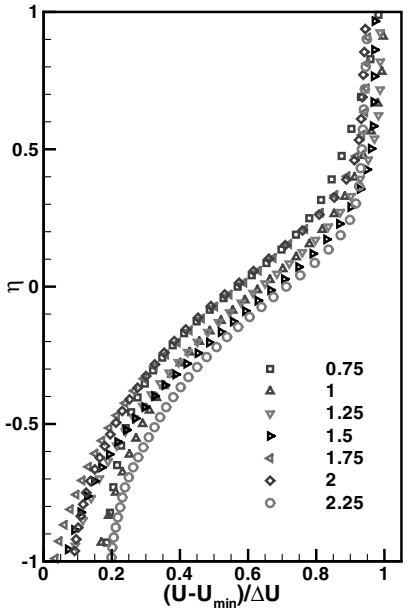

b) $M_\infty = 0.70$

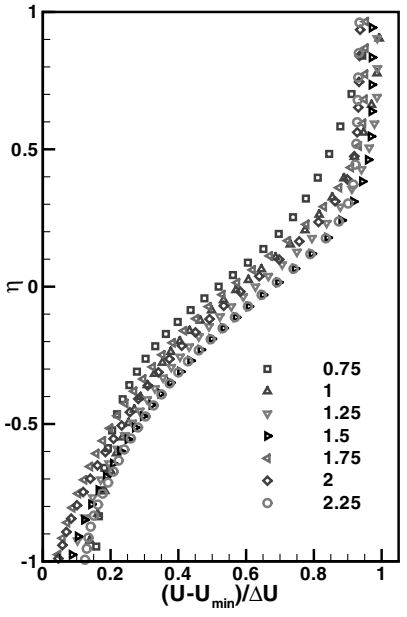

c) $M_\infty = 0.91$

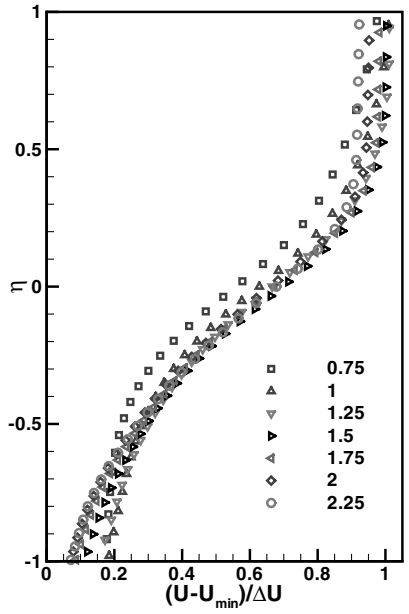

d) $M_\infty = 1.05$

Fig. 13 Time-averaged base-flow behavior; longitudinal velocity profiles in self-similar coordinates for several X/R locations.

several additional simulations in the supersonic regime and found the base-pressure fluctuations to rapidly be damped once $M_\infty > 1$. It illustrates the fact that both the mean and the fluctuating part of the base pressure are very sensitive to the freestream Mach number in the transonic regime.

The properties of the separated flow are now assessed. In particular, the time-averaged behavior of the mixing layer was investigated by plotting the evolution of the vorticity thickness δ_w, which reads as follows:

$$\delta_w = \frac{U_{\max} - U_{\text{low}}}{\max(\partial U/\partial y)} \tag{2}$$

Figure 12 presents the vorticity-thickness evolution for the four Mach numbers. The evolution of δ_w appears independent of M_∞. Three distinct trends can be observed up to the rear stagnation point. The first region just after separation extends on approximately $0.3X/L_R$ and corresponds to the initial part of the mixing layer, in which instabilities develop. Moving downstream, $\mathrm{d}\delta/\mathrm{d}x$ increases until reaching a value equal to 0.38, due to the coherent structure growth. At $X/L_R \sim 0.80$, a strong change in the mixing-layer evolution is observed. The vorticity thickness becomes nearly constant until the rear stagnation point is reached. This shift in the trend of growth rate is due to the appearance of an adverse pressure gradient when the flow starts to realign with the axis as observed in Fig. 3.

The behavior of the near-wake was further investigated by plotting the streamwise velocity profiles at several x/R stations downstream of the base in self-similar coordinates [54] for all Mach numbers. Despite strong departure from equilibrium conditions, due to the separation process, the flow appears to be in a self-similar state regardless of the investigated Mach number, as shown in Fig. 13. The slight discrepancies observed in the lower side of the profiles can be attributed to the variations in the backflow velocity, depending on the streamwise location.

The influence of the Mach number was also investigated by plotting the velocity profile at a given downstream location for all cases (Fig. 14). The different plots fit very well, except for the higher Mach number, for which differences appear in the reverse flow area approaching the axis (up to a factor of 2 for $r/R = 0$). However, the use of such coordinates appears to be well suited to compare such separated flows.

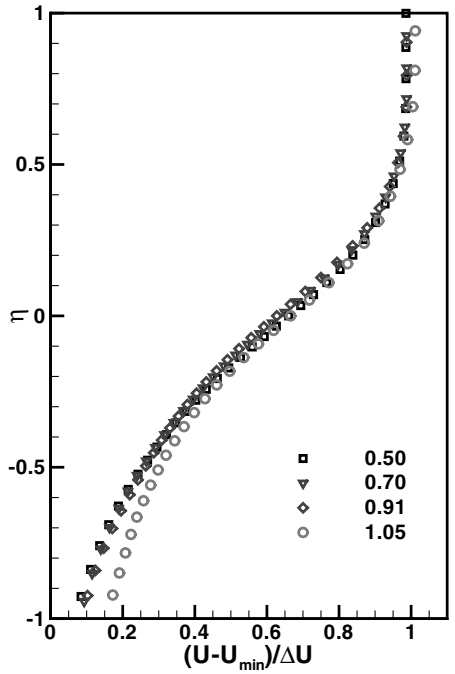

Fig. 14 Influence of the Mach number in self-similar coordinates ($X/R = 1.25$).

The self-similar properties of the turbulent field were also assessed. An example of such results is given in Fig. 15, which shows the profiles of velocity fluctuations and of the turbulent kinetic energy k at a given streamwise station. The radial evolution of the streamwise velocity fluctuations appears quite similar, despite weak discrepancies approaching the axis. For the radial and tangential components, more pronounced variations are encountered (see Figs. 15b and 15c). The magnitude of both $v^2_{\text{rms}}/\Delta U^2$ and $w^2_{\text{rms}}/\Delta U^2$ ratios are found to decrease with M_∞ for a given streamwise coordinate. Such behavior reveals an increase of the anisotropy of the turbulent field as the freestream Mach number is increased.

To get further insight into the dependence of the velocity fluctuations upon the Mach number, the longitudinal evolution of the velocity fluctuations and the turbulent kinetic energy maxima at the peak Reynolds stress location were plotted in Fig. 16. Once scaled by the freestream velocity, the fluctuation evolution behaves quite independently from the M_∞ value in the range of parameters investigated in the present study. It is observed that the maximum of fluctuations is reached upstream of the rear stagnation, which is in accordance with previous turbulent separated flow studies. The peak magnitude of $u_{\text{rms}}/U_\infty \sim 0.16$ is in good agreement with other studies dealing with planar shear layers [55–58]. Both radial and transverse components values are higher than those encountered in more fundamental work about separated flows. It is not clear if this is a consequence of the axisymmetry of the mixing layer or to the addition of the boat-tail section, which influences the streamline curvature behind the base and alters the fluctuations magnitude (this is the case in the supersonic regime, in which radial fluctuations levels increase with the addition of a boat tail [59], compared with the blunt-base case). However, slight discrepancies can be observed between the $M_\infty = 1.05$ case and the other simulations. The anisotropy of the fluctuations seems to be enhanced in the supersonic regime (as previously observed for the profile in self-similar coordinates). The streamwise fluctuation component increases and both the vertical and transverse components decrease, at least in the recompression region and in the developing wake. Moreover, the fluctuations seem to immediately react to the extra strain rate, due to the recompression when streamlines realign with the flow axis. The increase of the anisotropy and the sensitivity of the turbulence field toward the recompression area are two properties of supersonic free shear layers [60].

Instantaneous Features

At freestream conditions such as those investigated in the present work, unsteadiness appears both on the projectile body and in the near-wake. Numerical schlieren visualizations are plotted in Fig. 17 for the different Mach numbers investigated. For both subsonic cases, visualizations are very similar, in accordance with the observations made during the investigation of the time-averaged results. The only differences occur at the nose and at the geometrical slope shift on the body. In the transonic regime at $M_\infty = 0.91$, expansion waves form at both the ogive-cylinder and cylinder-boat-tail junctions. Behind these areas, shocks responsible for the higher pressure drag appear on the cylinder and the boat tail. These shocks are unsteady and oscillate at a Strouhal number St_D with $St_D = f \cdot D/U_\infty = 0.03$. For the $M_\infty = 1.05$ case, a conical shock originates at the nose, due to the supersonic incoming freestream velocity. The expansion fans are more clearly defined than in the previous case, due to a reinforcement of the pressure gradient. The boat-tail section exhibits a recompression region all over its length. In the near wake, shocks occur in the reattachment region, due to the realignment of the axisymmetric mixing layer with the axis.

Further insight into the near-wake dynamics is achieved by plotting the Q criterion [61], to highlight the existence of the coherent structures in the free annular mixing layer and in the developing wake. This criterion allows for investigating the region in which the rotation rate $\|\Omega\|$ exceeds the strain rate $\|S\|$ and expresses as follows:

$$Q = -\tfrac{1}{2}(\|S\| - \|\Omega\|) \tag{3}$$

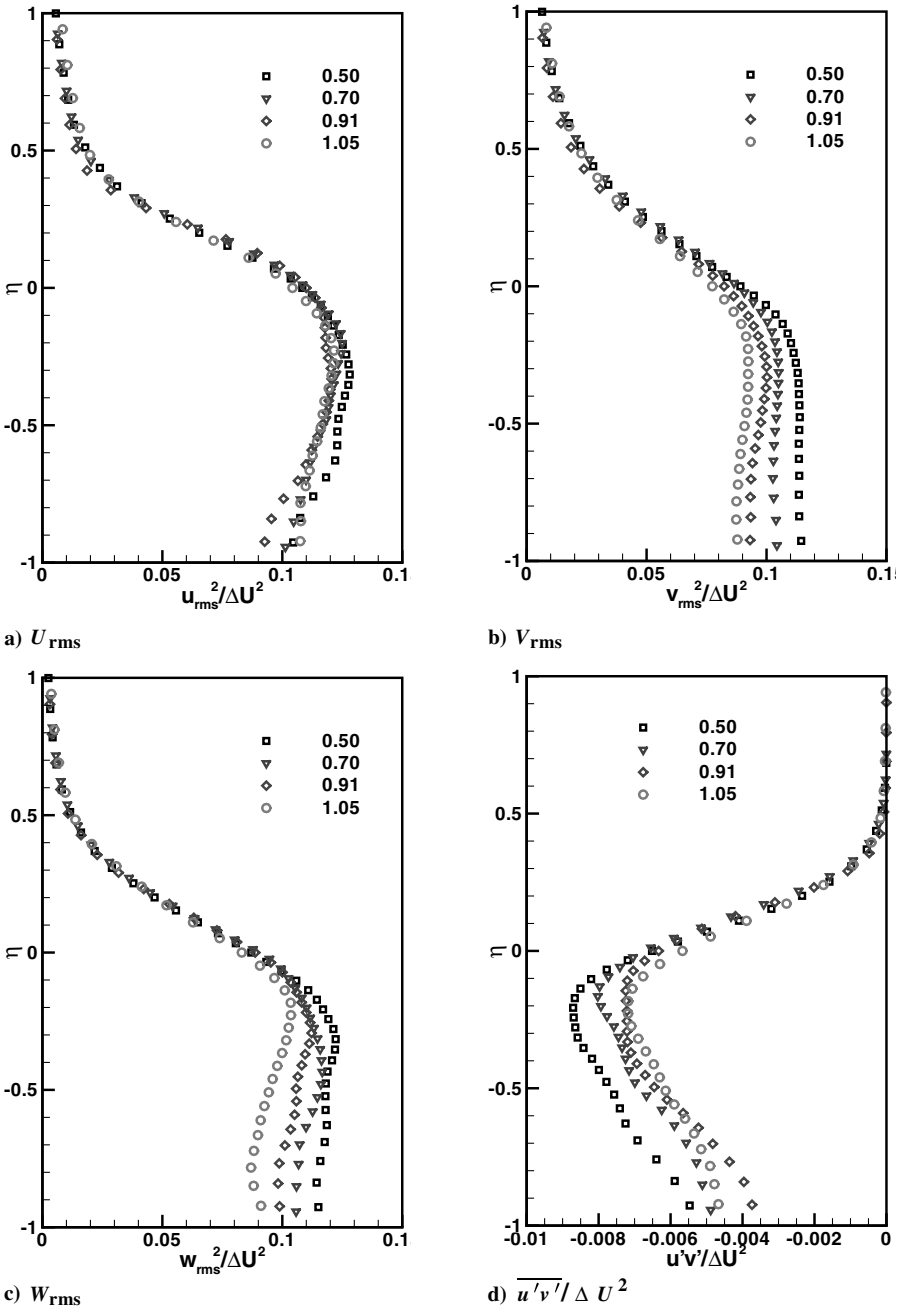

a) U_{rms} b) V_{rms}

c) W_{rms} d) $\overline{u'v'}/\Delta U^2$

Fig. 15 Time-averaged base-flow behavior; turbulence statistics profiles in self-similar coordinates ($X/R = 1.25$).

Figure 18 presents an isosurface of Q with the streamwise derivative of the density. In all of the ZDES simulations, eddies with strong azimuthal coherence can be seen just upstream of the separation. These vortices are due to the instability process of the free mixing layer. After being convected downstream, these structures break down as they pass through the recompression region. A wide range of turbulent scales are thus created and hairpin vortices, which are a characteristic feature of shear flows, are observed in the developing wake. One can notice that the destabilization process of the azimuthal vortices appears at a downstream location for the lower Mach number cases. However, Fig. 18 highlights the fact that the instability phenomena is quite independent of the freestream Mach number in the range investigated in the present study. This result is in accordance with fundamental mixing-layer analyses [45,46], which have demonstrated that the parameter required to scale the mixing-layer properties is not M_∞, but the convective Mach number.

These studies have demonstrated that the classical Kelvin–Helmholtz instability is dominant when M_c is lower than 0.6, leading to bidimensional eddies (or with strong azimuthal coherence for the annular mixing layer). When $0.6 < M_c < 1$, the amplification rate of 2-D perturbations decreases and oblique modes appear. For $M_c > 1$, the structures are highly three-dimensional with a weak amplification rate. The convective Mach number was calculated in the present cases just downstream of the separation. The results are shown in Table 2. In all cases, M_c is smaller than 0.6, which justifies the observation of the same instability type in the present simulations. The convective velocity of the structures can also be derived from the isentropic model of the convective Mach number. The estimation of U_c/U_∞, which is approximately equal to 0.5 for all of the simulations, is in accordance with other studies dealing with planar shear layers [62,63] or separated flows, such as those encountered in backward-facing step flows [64–67].

Spectral Analysis

Further insight into the dynamics of the separated flow can be achieved by using sensors at the base. Unsteady loads can occur on the base, due to quite large pressure fluctuations. To investigate this

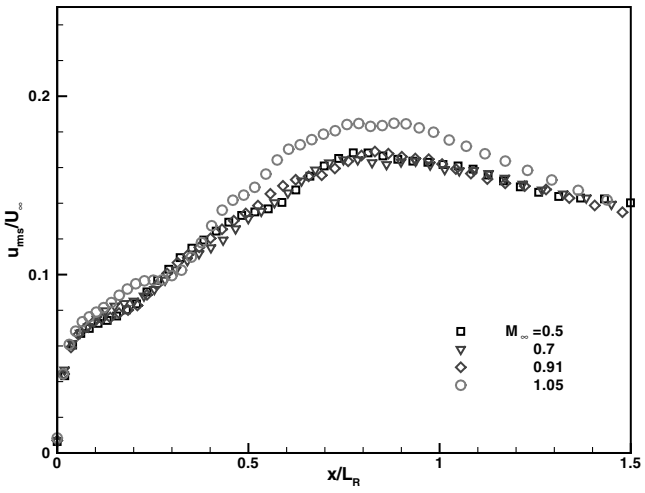

a) U_{rms}

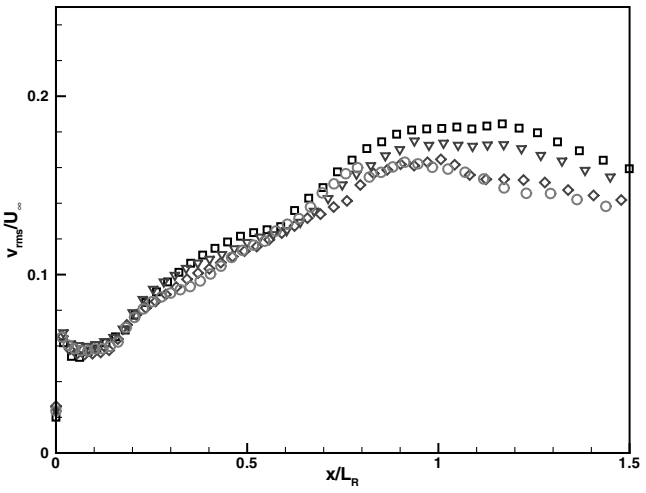

b) V_{rms}

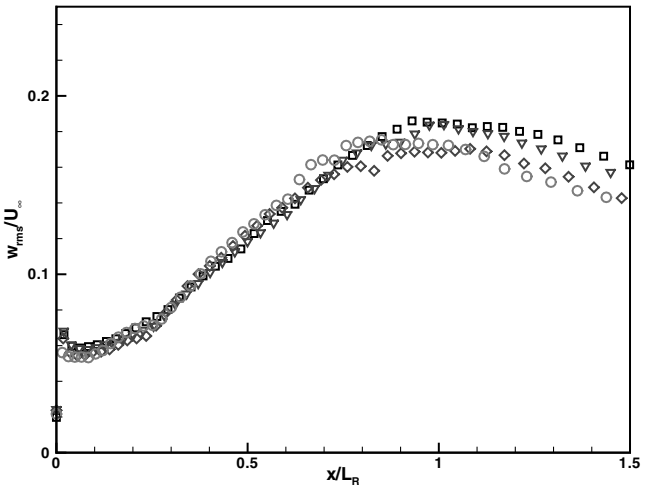

c) W_{rms}

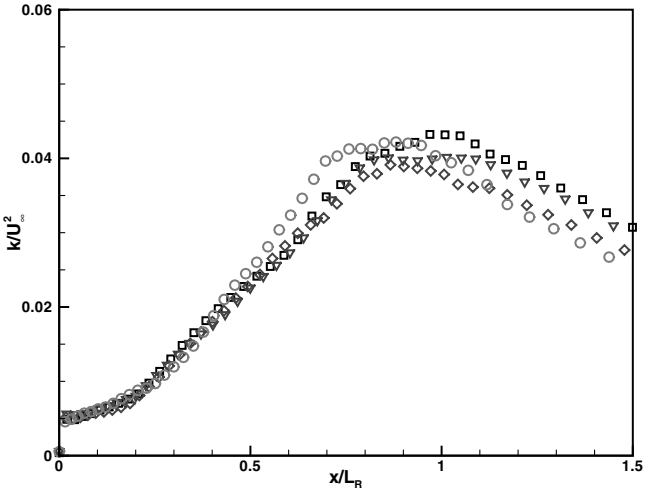

d) k

Fig. 16 Time-averaged base-flow behavior; maximum of turbulence fluctuations and maximum of turbulent kinetic energy.

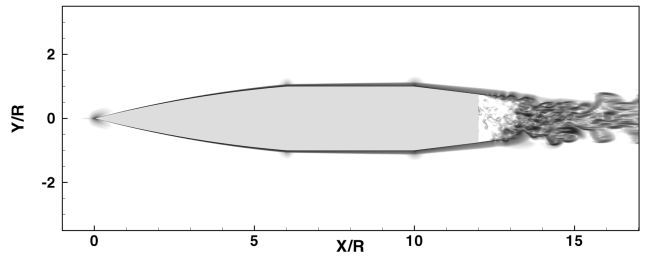

a) $M_\infty = 0.50$

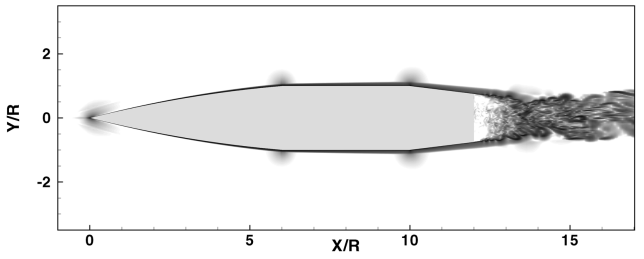

b) $M_\infty = 0.70$

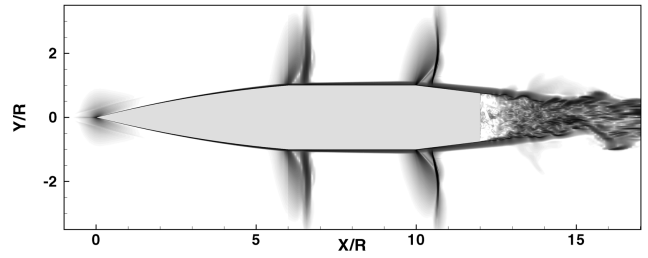

c) $M_\infty = 0.91$

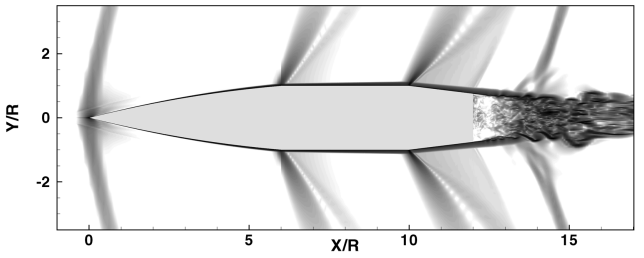

d) $M_\infty = 1.05$

Fig. 17 Pseudo-schlieren visualization; isocontours of $\|grad(\rho)\|$.

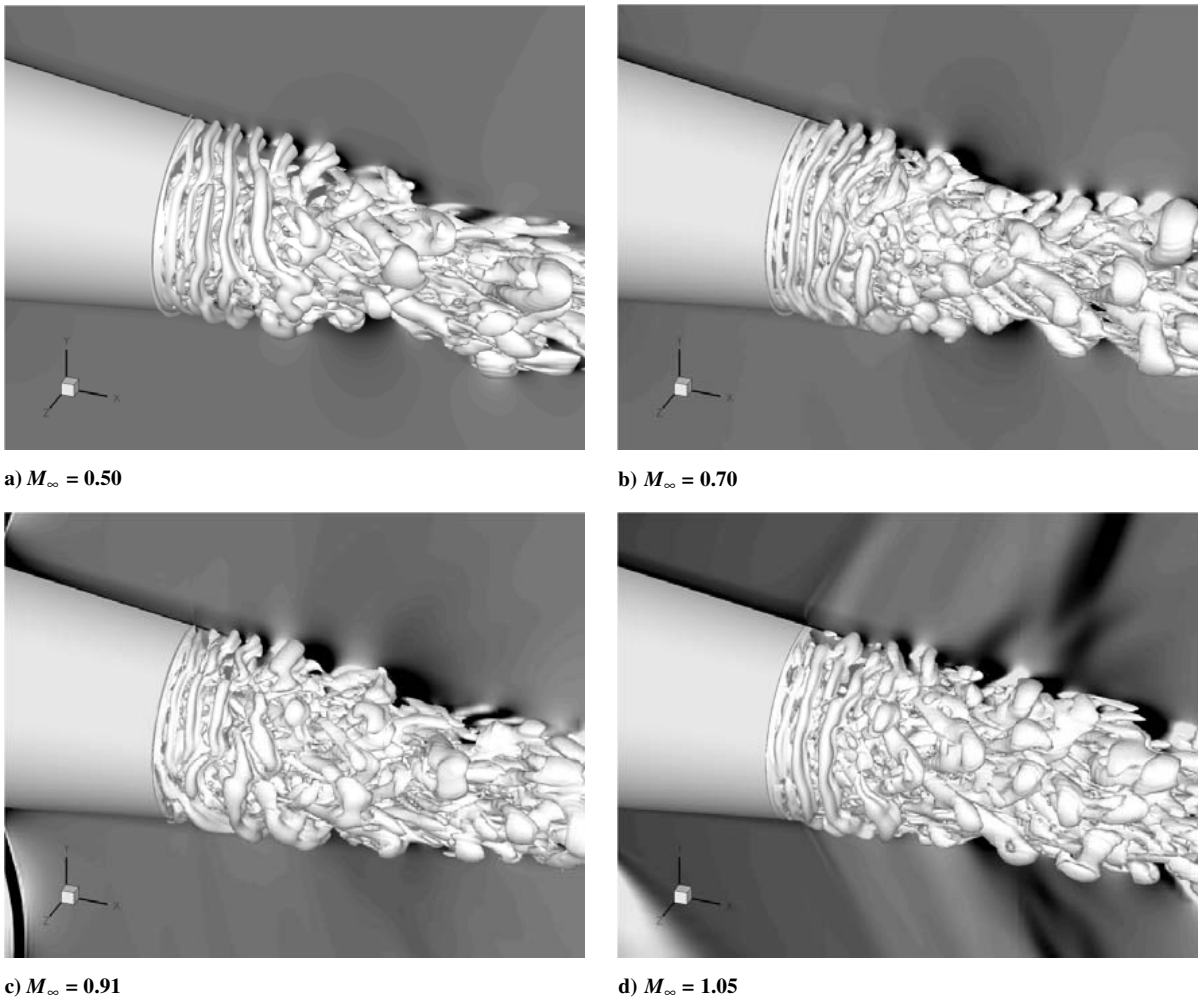

a) M_∞ = 0.50 b) M_∞ = 0.70

c) M_∞ = 0.91 d) M_∞ = 1.05

Fig. 18 Isocontours of $Q = 1(U_\infty/D)^2$ criterion and the longitudinal derivative of the density.

issue, time series of base pressures were obtained for all of the ZDES simulations. The main goal of the present section is to investigate the frequency content of the pressure fluctuations on the base and to evidence the influence of the Mach number on the characteristic frequencies of the base-pressure fluctuations. Not many studies [48,49,52,53] were devoted to the analysis of base-pressure fluctuations, and further studies are required to get a better knowledge of such unsteadiness.

Figure 19 presents the nondimensionalized base-pressure-fluctuations spectra at the base center location as a function of the Strouhal number St_D using the Welch [68] periodogram method. For $M_\infty = 0.5$, three distinct peaks can be evidenced for St_D, equal to 0.054, 0.117, and 0.270. Although not shown here for the sake of clarity, unsteady data along a whole base radius and in the separated flow were investigated. It is interesting to note that these three frequencies are more clearly visible in the outer part of the base radius and can also be observed in the initial part of the boundary layer separating from the base. However, these frequencies are at least inferior to one order, compared with the fundamental Kelvin-Helmholtz frequency, which is equal to $St_D \sim 3.84$ in the initial stage of the shear layer (observed on both velocity and pressure spectra). Indeed, the instability frequency depends on the intrinsic shear-layer characteristics. Thus, a more appropriate scaling is needed. Then, $St_D \sim 3.83$ corresponds to $St_{\delta_\omega} \sim 0.138$, where $St_{\delta_\omega} = f\delta_\omega/U_c$. This value agrees well with the estimation given by a two-dimensional linear stability analysis of a planar shear layer [69]:

$$f_{\mathrm{KH}} \sim 0.135(U_c/\delta_\omega) \tag{4}$$

The frequencies observed at the base center are thus too low to scale with the shear-layer instability frequency. The $St_D = 0.27$ is

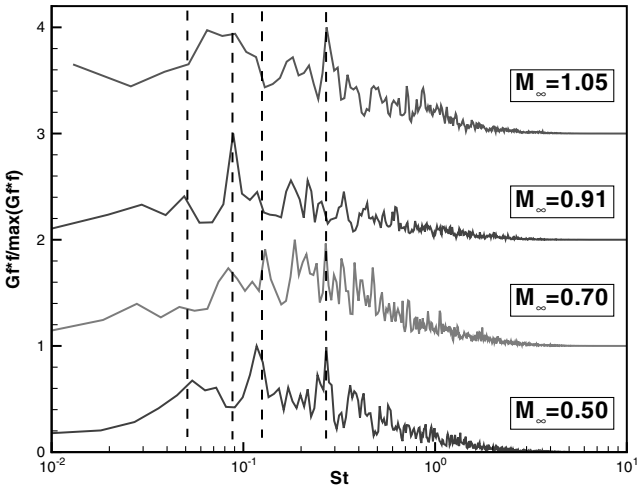

Fig. 19 Base pressure fluctuations spectra.

thought to be characteristic of large-scale structures such as those observed in the vortex-shedding phenomenon, whereas the two lower frequencies can be attributed to a global behavior of the recirculating flow. In addition, the existence of a major peak at $St_D \sim 0.12$ at the outer part of the base could be the signature of a flapping motion of the shear layer, such as that encountered in backward-facing step flows [64,70,71]. For the $M_\infty = 0.70$ case, peaks appear to be less pronounced, but a phenomenon with a reduced frequency $St_D = 0.13$ appears, despite a more important high-frequency fluctuation content. The base-pressure fluctuations

also exhibit a nonnegligible contribution at $St_D = 0.091$. It is obvious that such a phenomenon occurs in the transonic regime, because a clear peak around $St_D \sim 0.09$ is observed.

The last spectrum concerns the supersonic case. A broadband low-frequency contribution is observed for $0.05 < St_D < 0.1$. However, a major peak also occurs for $St_D \sim 0.28$, similar to those already observed for the two lower M_∞ cases.

Unfortunately, a detailed analysis of such spectra proves to be insufficient to evidence the origin of the observed low-frequency phenomenon. A further investigation of the whole time series in the separated flowfield is thus required to get additional insight into the comprehension of such low frequencies at the base.

Conclusions

The scope of the present study was to investigate the influence of the turbulence-modeling strategy on the computed flowfields around a classical projectile shape and to provide some additional data relative to the separated flow physics. The flow around a secant-ogive-cylinder boat-tail configuration was thus investigated in both the subsonic and transonic regimes with the use of a zonal-detached-eddy simulation on a 7×10^6 point grid and compared with results obtained with a statistical approach. The grid requirements to capture a RANS boundary layer are maintained when the hybrid method is used, as far as the wall-pressure measurements are concerned. The use of a RANS methodology appears to be well suited for computing the attached flowfield around the projectile body, because the pressure gradient and the shock locations (in the transonic regime) are well captured. The separated flow was then investigated. In the present simulations, the Spalart–Allmaras model poorly predicts some classical features of base flows, such as the constant pressure on the base surface or the location at which the maximum backflow amplitude is reached, contrary to the hybrid calculations. These promising results allow for investigating the base-flow physics more accurately. Some fundamental properties concerning the centerline velocity of axisymmetric base flows are retrieved, such as the intensity and the location of the maximum reverse backflow. However, the pressure coefficient is found to deviate from the blunt-base-flow configuration until the rear stagnation is reached. Moreover, the base-pressure coefficient proves to be not directly linked to the backflow extent in the transonic range. The recirculation length is found to slightly increase with the freestream Mach number, whereas a minimum of base pressure is encountered at $M_\infty = 0.91$, from strong transonic effects. The magnitude of base-pressure fluctuations is found to increase with M_∞ and its profile, which is nearly constant for $M_\infty = 0.5$, exhibits a maxima at the base center for higher M_∞. The near wake rapidly becomes self-similar, even in the recirculating flow, whatever the freestream conditions used in the present study. Slight variations of the velocity fluctuations between the four cases are observed, which may be attributed to the increase of the anisotropy with the freestream Mach number. Finally, sensors were used to investigate the spectral content of the pressure fluctuations at the base. The spectra exhibit the existence of some low-frequency movement, characteristic of a global motion of the entire recirculating bubble. This result corroborates previous backward-facing step studies in which flapping motion of the shear layer was observed and reveals that such a phenomenon also occurs in axisymmetric base flows. Unfortunately, the lack of an extensive experimental database is a major difficulty for validating new hybrid approaches and reveals the current needs of the aeroballistic community. Such methodologies require quantitative measurements of the turbulent field through the use of experimental particle image velocimetry or laser Doppler velocimetry devices. The present contribution could be a start toward assembling such data for this problem. Further work will now be devoted to more realistic projectile flight conditions. In particular, the combination of the angle of attack and of the body rotation, leading to the widely known Magnus force, will be investigated with the use of a zonal-detached-eddy simulation approach to evidence the influence of the body rotation on the flowfield.

Acknowledgments

This study was partly funded by Giat Industries within the framework of ONERA/Giat Industries cooperation.

References

[1] Nietubicz, C. J., Sturek, W. B., and Heavey, K. R., "Computations of Projectile Magnus Effect at Transonic Velocities," *AIAA Journal*, Vol. 23, No. 7, 1983, pp. 998–1004.

[2] Silton, S. I., "Navier-Stokes Computations for a Spinning Projectile from Subsonic to Supersonic Speeds," AIAA Paper 2003-3936, 2003.

[3] Thépot, R., "PEA Magnus—Etude Numérique de l'Effet Magnus sur un Projectile en Rotation (Modélisation Baldwin–Lomax)—Comparaison aux Résultats d'Essais en Soufflerie," ONERA, Technical Rept. RT/261/05349 DAAP, 2003.

[4] Thépot, R., Paulo d'Espiney, and Pillon, J.-P., "PEA Magnus—Etude Numérique de l'Effet Magnus sur un Projectile en Rotation. Travaux Complémentaires (Modélisation Spalart–Allmaras)—Conditions de Vol," ONERA, Technical Rept. RT/262/05349 DAAP, 2003.

[5] Cummings, R. M., Yang, H. T., and Oh, Y. H., "Supersonic, Turbulent Flow Computation and Drag Optimization for Axisymmetric Afterbodies," *Computers and Fluids*, Vol. 24, No. 4, 1995, pp. 487–507.

[6] Péchier, M., Guillen, P., and Cayzac, R., "Magnus Effect Over Finned Projectiles," *Journal of Spacecraft and Rockets*, Vol. 38, No. 4, 2001, pp. 542–549.

[7] Simon, F., Deck, S., Guillen, P., and Cayzac, R., "Numerical Simulations of Projectile Base Flow," AIAA Paper 2006-1116, 2006.

[8] Spalart, P. R., and Allmaras, S. R., "A One Equation Turbulence Model for Aerodynamic Flows," AIAA Paper 92-0439, 1992.

[9] Spalart, P. R., and Allmaras, S. R., "A One Equation Turbulence Model for Aerodynamic Flows," *La Recherche Aérospatiale*, Vol. 1, No. 1, 1994, pp. 5–21.

[10] Baldwin, B., and Lomax, H., "Thin-Layer Approximation and Algebraic Model for Separated Turbulent Flows," AIAA Paper 78-0257, 1978.

[11] Cayzac, R., Carette, E., Champigny, P., Thépot, R., and Donneaud, O., "Analysis of Static and Dynamic Stability of Spinning Projectiles," *21st International Symposium on Ballistics*, edited by N. Burman, J. Anderson, and G. Katselis, Australian Dept. of Defence, Defence Science and Technology Organisation, 2004.

[12] DeSpirito, J., and Heavey, K. R., "CFD Computation of Magnus Moment and Roll Damping Moment of a Spinning Projectile," AIAA Paper 2004-4713, 2004.

[13] Simon, F., "Synthese Bibliographique des Méthodes de Contrôle Actif des Écoulements à l'Aide d'Actionneurs," ONERA, Technical Rept. RT1/09158 DAAP, 2004.

[14] Sahu, J., and Nietubicz, C. J., "Navier-Stokes Computations of Projectile Base Flow with and Without Base Injection," AIAA Paper 1983-224, 1983.

[15] Sahu, J., "Supersonic Flow Over Cylindrical Afterbodies with Base Bleed," AIAA Paper 1986-487, 1986.

[16] Dandberg, J., and Nietubicz, C., "Predicted Flight Performance of Base Bleed Projectiles," AIAA Paper 90-2069, 1990.

[17] Sahu, J., and Heavey, K. R., "Numerical Investigation of Supersonic Base Flow with Base Bleed," *Journal of Spacecraft and Rockets*, Vol. 34, No. 1, 1997, pp. 62–69.

[18] Kaurinkoski, A., and Hellsten, P., "Numerical Simulation of a Supersonic Base- Bleed Projectile with Improved Turbulence Modeling," *Journal of Spacecraft and Rockets*, Vol. 35, No. 5, 1998, pp. 606–611.

[19] Bournot, H., Daniel, E., Lepalec, G., and Cayzac, R., "Numerical Simulation of Base-Bleed Effect in a Supersonic Flow over a Cylindrical Afterbody," *21st International Symposium on Ballistics*, edited by N. Burman, J. Anderson, and G. Katselis, Australian Dept. of Defence, Defence Science and Technology Organisation, 2004.

[20] Kruiswyk, R. W., and Dutton, J. C., "An Experimental Investigation of the Effects of a Base Cavity on the Near-Wake Flowfield of a Body at Subsonic and Transonic Speeds," AIAA Paper 1989-210, 1989.

[21] Molezzi, M. J., and Dutton, J. C., "Study of the Near-Wake Structure of a Subsonic Base Cavity Flowfield Using PIV," 24th AIAA Fluid Dynamics Conference, Orlando, FL, AIAA Paper 1993-3040, 1993.

[22] Sahu, J., "Unsteady Numerical Simulations of Subsonic Flow over a Projectile with Jet Interaction," AIAA Paper 2003-1352, 2003.

[23] Sahu, J., "Unsteady CFD Modeling of Aerodynamic Flow Control over a Spinning Body with Synthetic Jet," AIAA Paper 2004-0747, 2004.

[24] Sahu, J., "Coupled CFD and Rigid Body Dynamics Modeling of a Spinning Body with Flow Control," AIAA Paper 2004-2317, 2004.

[25] Sahu, J., and Heavey, K. R., "Numerical Simulations of Micro-Adaptative Flow Control for a Spinning Projectile at Subsonic Speeds," *21st International Symposium on Ballistics*, edited by N. Burman, J. Anderson, and G. Katselis, Australian Dept. of Defence, Defence Science and Technology Organisation, 2004.

[26] Rinehart, C., McMichael, J. M., and Glezer, A., "Transitory Flow and Force Development on a Body of Revolution Using Synthetic Jet Actuation," AIAA Paper 2003-0618, 2003.

[27] McMichael, J., Lovas, A., Plostins, P., Sahu, J., Bown, G., and Glezer, A., "Microadaptative Flow Control Applied to a Spinning Projectile," AIAA Paper 2004-2512, 2004.

[28] Motallebi, F., and Norbury, J. F., "The Effect of Base Bleed on Vortex Shedding and Base Pressure in Compressible Flow," *Journal of Fluid Mechanics*, Vol. 110, Sept. 1981, pp. 272–292.

[29] Deck, S., Duveau, P., d'Espiney, P., and Guillen, P., "Development and Application of Spalart Allmaras One Equation Turbulence Model to Three-Dimensional Supersonic Complex Configurations," *Aerospace Science and Technology*, Vol. 6, No. 3, 2002, pp. 171–183.

[30] Deck, S., Garnier, E., and Guillen, P., "Turbulence Modelling Applied to Space Launcher Configurations," *Journal of Turbulence*," Vol. 3, No. 57, 2002, pp. 1–21.

[31] Spalart, P., Jou, W. H., Strelets, M., and Allmaras, S. R., "Comments on the Feasibility of LES for Wings and on a Hybrid RANS/LES Approach," *Proceedings of the 1st AFOSR International Conference on DNS/LES*, Gryden Press, Columbus, OH, 1997, pp. 137–147.

[32] Shur, M., Spalart, P. R., Strelets, M., and Travin, A., "Detached-Eddy Simulation of an Airfoil at High Angle of Attack," *4th International Symposium on Engineering Turbulence Modelling and Measurements*, Elsevier Science, Oxford, England, U.K., 1999, pp. 669–678.

[33] Deck, S., "Zonal-Detached Eddy Simulation of the Flow Around a High Lift Configuration," *AIAA Journal*, Vol. 43, No. 11, 2005, pp. 2372–2384.

[34] Deck, S., "Numerical Simulation of Transonic Buffet over a Supercritical Airfoil," *AIAA Journal*, Vol. 43, No. 7, 2005, pp. 1556–1566.

[35] Simon, F., Deck, S., Guillen, P., and Sagaut, P., "Reynolds-Averaged Navier-Stokes/Large-Eddy Simulations of Supersonic Base Flow," *AIAA Journal*, Vol. 44, No. 11, 2006, pp. 2578–2590.

[36] Menter, F. R., Kuntz, M., and Bender, R., "A Scale-Adaptive Simulation Model for Turbulent Flow Predictions," AIAA Paper 03-0767, 2003.

[37] Spalart, P. R., Deck, S., Shur, M. L., Squires, K. D., Strelets, M. Kh., and Travin, A., "A New Version of Detached-Eddy Simulation, Resistant to Ambiguous Grid Densities," *Theoretical and Computational Fluid Dynamics*, Vol. 20, July 2006, pp. 181–195.

[38] Sagaut, P., Deck, S., and Terracol, M., *Multiscale and Multiresolution Approaches in Turbulence*, Imperial College Press, London, 2006.

[39] Kayser, L. D., and Whiton, F., "Surface Pressure Measurements on a Boattailed Projectile Shape at Transonic Speeds," U.S. Army Ballistic Research Laboratory ARBRL-MR-03161, Aberdeen Proving Ground, MD, Mar. 1982.

[40] Montigny-Rannou, F., "Mailleur MESH3D: Manuel d'Utilisation Ver. MESH3D-1.2," ONERA Technical Rept. RT1/6179 DSNA/N, Dec. 1999.

[41] Deck, S., "Pea Cacv: Tâche 3.3.1.2. Simulation Numérique d'un Écoulement de Culot avec Différentes Modélisations de la Turbulence," ONERA Technical Rept. RT1/09509 DAAP, Feb. 2006.

[42] Deck, S., and Garnier, E., "Detached and Large Eddy Simulation of Unsteady Side Loads over an Axisymmetric Afterbody," 5th European Symposium on Aerothermodynamics for Space Vehicles, Cologne, Germany, ONERA Paper TP 2005-37, 2004.

[43] Merz, R. A., Page, R. H., and Przirembel, G. C. E., "Subsonic Axisymmetric Near-Wake Studies," *AIAA Journal*, Vol. 16, No. 7, 1978, pp. 656–662.

[44] Délery, J., and Siriex, M., "Ecoulements de Culot," *l'Aérodynamique des Missiles*, LS-98, AGARD, Neuilly-sur-Seine, France, 1979, pp. 2–5.

[45] Bogdanoff, D. W., "Compressibility Effects in Turbulent Shear Layers," *AIAA Journal*, Vol. 21, No. 6, 1983, pp. 926-927.

[46] Papamoschou, D., and Roshko, A., "The Compressible Turbulent Shear Layer: An Experimental Study," *Journal of Fluid Mechanics*, Vol. 197, Dec. 1988, pp. 453–477.

[47] Simon, F., "Simulations Numériques Hybrides RANS/LES de l'Aérodynamique des Projectiles et Application au Contrôle des Ecoulements," Ph.D. Thesis, Univ. de Lille 1, Lille, France, 2007.

[48] Deprés, D., "Analyse Physique et Modélisation des Instationnarités dans les Ecoulements d'Arriére-Corps Transsoniques," Ph.D. Thesis, Univ. de la Méditerranée Aix-Marseille II, Marseille, France, 2003.

[49] Janssen, J. R., and Dutton, J. C., "Time-Series Analysis of Supersonic Base-Pressure Fluctuations," *AIAA Journal*, Vol. 42, No. 3, 2004, pp. 605–613.

[50] Forsythe, J. R., Hoffmann, K. A., Cummings, R. M., and Squires, K. D., "Detached-Eddy Simulation with Compressibility Corrections Applied to a Supersonic Axisymmetric Base Flow," *Journal of Fluids Engineering*, Vol. 124, Dec. 2002, pp. 911–923.

[51] Kayser, L. D., "Base Pressure Measurements on a Projectile Shape at Transonic Speeds," U.S. Army Ballistic Research Laboratory ARBRL-MR-03353, Aberdeen Proving Ground, MD, Apr. 1984.

[52] Merz, R. A., "Subsonic Base Pressure Fluctuations," *AIAA Journal*, Vol. 17, No. 4, 1979, pp. 330–331.

[53] Kawai, S., "Computational Analysis of the Characteristics of High Speed Base Flows," Ph.D. Thesis, School of Engineering, Univ. of Tokyo, Tokyo, Japan, Feb. 2005.

[54] Jovic, S., "An Experimental Study of a Separated/Reattached Flow Behind a Backward-Facing Step, $Re_H = 37,000$," NASA, TM 110384, 1996.

[55] Goebel, S. G., and Dutton, J. C., "Experimental Study of Compressible Turbulent Mixing Layers," *AIAA Journal*, Vol. 29, No. 4, 1990, pp. 538–546.

[56] Samimy, M., and Elliot, G. S., "Effects of Compressibility on the Characteristics of Free Shear Flows," *AIAA Journal*, Vol. 28, No. 3, 1990, pp. 439–445.

[57] Urban, W. D., and Mungal, M. G., "Planar Velocity Measurements in Compressible Mixing Layers," *Journal of Fluid Mechanics*, Vol. 431, June 2001, pp. 189–222.

[58] Pantano, C., and Sarkar, S., "A Study of Compressibility Effects in the High-Speed Turbulent Shear Layer Using Direct Simulation," *Journal of Fluid Mechanics*, Vol. 451, Jan. 2002, pp. 329–371.

[59] Herrin, J. L., and Dutton, J. C., "Effect of a Rapid Expansion on the Development of Compressible Free Shear Layers," *Physics of Fluids*, Vol. 7, No. 1, 1995, pp. 159–171.

[60] Herrin, J. L., and Dutton, J. C., "The Turbulence Structure of a Reattaching Axisymmetric Compressible Free Shear Layer," *Physics of Fluids*, Vol. 9, No. 11, 1997, pp. 3502–3512.

[61] Jeong, J., and Hussain, F., "On the Identification of a Vortex," *Journal of Fluid Mechanics*, Vol. 285, Feb. 1995, pp. 69–94.

[62] Brown, G. L., and Roshko, A., "On Density Effects and Large Structure in Turbulent Mixing Layers," *Journal of Fluid Mechanics*, Vol. 64, July 1974, pp. 775–816.

[63] Morris, S. C., and Foss, J. F., "Turbulent Boundary-Layer to Single-stream Shear Layer: the Transition Region," *Journal of Fluid Mechanics*, Vol. 494, Oct. 2003, pp. 187–221.

[64] Heenan, A. F., and Morrison, J. F., "Passive Control of Pressure Fluctuations Generated by Separated Flows," *AIAA Journal*, Vol. 36, No. 6, 1990, pp. 1014–1022.

[65] Lee, I., and Sung, H. J., "Characteristics of Wall Pressure Fluctuations in Separated and Reattaching FLows over a Backward-Facing Step, Part 1: Time-mean Statistics and Cross-Spectral Analyses," *Experiments in Fluids*, Vol. 30, No. 3, 2001, pp. 262–272.

[66] Dejoan, A., and Leschziner, M. A., "Large-Eddy Simulation of Periodically Perturbed Separated Flow over a Backward-Facing Step," *International Journal of Heat and Fluid Flow*, Vol. 25, No. 4, 2004, pp. 581–592.

[67] Liu, Y. Z., Kang, W., and Sung, H. J., "Assessment of the Organization of a Turbulent Separated and Reattaching Flow by Measuring Wall Pressure Fluctuations," *Experiments in Fluids*, Vol. 38, No. 4, 2005, pp. 485–493.

[68] Welch, P. D., "The Use of Fast Fourier Transform for the Estimation of Power Spectra: A Method Based on Time Averaging over Short Modified Periodograms," *IEEE Transactions on Audio and Electroacoustics*, Vol. AU-15, No. 2, June 1967, pp. 70–73.

[69] Huerre, P., and Rossi, M., "Hydrodynamic Instabilities in Open Flows," *Hydrodynamics and Nonlinear Instabilities*, Cambridge Univ. Press, New York, 1998, pp. 81–214.

[70] Hudy, L. M., Naguib, A. M., and Humphreys, W. M., "Wall-Pressure-Array Measurements Beneath a Separating/Reattaching Flow Region," *Physics of Fluids*, Vol. 15, No. 3, 2003, pp. 706–715.

[71] Naguib, A. M., and Hudy, L. M., "Stationary and Propagating Low-frequency Wall-pressure Disturbances in a Separating/Reattaching Flow," AIAA Paper 2003-1126, 2003.

P. Givi
Associate Editor